Seventh International Conference on CFD in the Minerals and Process Industries
CSIRO, Melbourne, Australia
9-11 December 2009

NUMERICAL STUDIES OF HIGH REYNOLDS NUMBER FLOW PAST A STATIONARY AND ROTATING SPHERE

Eric K. W. POON[1], Gianluca IACCARINO[2], Andrew S. H. OOI[1] and Matteo GIACOBELLO[3]

[1] Department of Mechanical Engineering, University of Melbourne, Parkville, Victoria 3010, AUSTRALIA
[2] Center of Turbulence Research, CTR, Building 500, Stanford University, Stanford, CA 94305-3035, USA
[3] Air Vehicle Division, Defence Science & Technology Organisation, 506 Lorimer Street, Fisherman Bend, Victoria 3207, AUSTRALIA

ABSTRACT

Numerical solutions for the flow past stationary and rotating spheres at Re = 250, 1,000 and 10,000 are presented. Calculations are performed using the finite volume solver CDP developed at Stanford University. The solver is verified by simulating the uniform flow past a rotating sphere at Re = 250. The numerical results show good agreement with numerical data available in the open literature. Computations are also conducted to study the turbulent flow past a stationary and rotating sphere at Re = 1,000 and 10,000. The axis of rotation is orientated in two of the major axis directions, $\alpha = 0$ (streamwise rotation) and $\alpha = \pi/2$ (transverse rotation). Non-dimensional rotation rate Ω^* = 1 (maximum surface velocity normalized by the freestream velocity) is considered. The effect of rotating the sphere in either the streamwise or transverse direction on the wake structures and hydrodynamic forces are analysed. A complete picture of the physics associated with a rotating sphere can therefore be revealed.

NOMENCLATURE

d	diameter of the sphere
$\boldsymbol{e}$	unit vector
m	computer memory
n	face normal direction
p	pressure
$\mathbf{u}$	velocity
(u_x, u_y, u_z)	Cartesian velocity non-dimensionalised by U_∞
i	index variables
(x, y, z)	Cartesian coordinates non-dimensional by d
(r, θ, ϕ)	Spherical coordinates non-dimensional by d
A	face area of the control volume
V	volume of the control volume
C_s	Smagorinsky model coefficient
C_d	dynamic Smagorinsky model coefficient
C_D	drag coefficient
C_L	lift coefficient
N	number of grid points
Re	Reynolds number based on sphere diameter
St_1	vortex shedding Strouhal number
St_2	shear layer Strouhal number
U_∞	freestream velocity magnitude
α	rotation axis angle
λ_2	intermediate eigenvalue of the tensor $S_{kj}S_{ik} + \Omega_{kj}\Omega_{ik}$
ω	vorticity
Δt	dimensional timestep
Ω	dimensional rotational speed
Ω^*	non-dimensional rotation rate, $\Omega^* = \Omega d/2$
CDP	finite volume code named after Charles David Pierce, Stanford University
DNS	direct numerical simulation
LES	large eddy simulation
SGS	subgrid-scale
$[\ ]_p$	a value associated with the control volume
$[\ ]_{nbr}$	an adjacent control volume sharing the same face
$[\ ]_f$	common face of two control volume
$\vert\ \vert$	magnitude of a term

INTRODUCTION

In industrial applications such as engine combustion and, mineral and chemical processing the transport of particulate can be considered as a solid spherical body submerged in an incompressible Newtonian fluid. In order to predict and study the trajectory of the particulate, it is important to understand the flow structures and how they influence the hydrodynamic forces on the particulate.

Significant research effort has been made into studying the flow past a stationary sphere over a wide range of Reynolds numbers both experimentally (Achenbach, 1973; Taneda 1956; Taneda, 1998) and numerically (Constantinescu and Squires, 2004; Johnson and Patel, 1999; Mittal, 1999; Tomboulides and Orszag, 2000; Ploumhans *et. al.* (2002); Yun *et. al.*, 2006). However, numerical studies for a rotating sphere have only considered low Reynolds numbers ($Re \leq 500$) situations. The flow past a rotating sphere has been studied previously with the sphere rotating in either the streamwise or transverse directions. A streamwise rotating sphere was observed to bring forward the separation point in the laminar boundary layer regime (Hoskin, 1955). This is due to the additional adverse pressure gradient introduced by the rotating surface of the sphere. Luthander and Rydberg (1935) also observed a change in critical Reynolds number where the drag coefficient sharply decreases. Kim and Choi (2002) performed direct numerical simulations of flow past a streamwise rotating sphere for Re = 100, 250 and 300. They discovered that at Re = 250 and 300, the flow structures become "frozen" for certain rotation rates. In this regime the flow structures appear to be stationary if the coordinate system is rotating at the same angular velocity as the flow structures.

The induced "Robins-Magnus" lift force associated with transversely rotating sphere has attracted more attention than a streamwise rotating sphere. Experiments and numerical studies have been performed in the laminar Reynolds numbers regime ($0 < Re \leq 300$), and several different lift and drag correlations were derived by different researchers. Recently, Giacobello *et. al.* (2009) performed DNS at moderate Reynolds number using a Fourier-Chebyshev spectral collocation method. Their results are in good agreement with the experimental result by Rubinow and Keller (1961) and You *et. al.* (2003), but the lift coefficient was observed to be higher than Kurose and Komori (1999) and Niazmand and Renksizbukut (2003). As Reynolds number increases ($O(10^4)$), Maccoll (1928) observed a negative "Robins-Magnus" lift force for low rotational rates. The effect vanishes as the rotational rate increases. The negative "Robins-Magnus" lift force was also observed by Davies (1949) which he attributed this behaviour to the laminar-turbulent boundary transition.

In order to extend the understanding of a sphere's trajectory due to rotation, the flow past a stationary sphere and rotating sphere is investigated in the turbulence regime at Re = 1,000 and 10,000.

NUMERICAL METHOD

Governing Equations

The finite volume solver CDP used in this study is developed at Stanford University and is named after its original creator Charles David Pierce (Mahesh *et. al.*, 2004; Ham and Iaccarino, 2004). The fluids motion is described by incompressible Navier-Stokes equations

$$\frac{\partial \mathbf{u}}{\partial t} + \mathbf{u} \cdot \nabla \mathbf{u} = -\nabla p + \frac{1}{Re} \nabla^2 \mathbf{u}, \quad (1)$$

$$\nabla \cdot \mathbf{u} = 0 . \quad (2)$$

The primitive variables in these equations are the velocity vector, **u**, and the pressure scalar, p. Jiménez (2003) estimated that in order to numerically solve (1) and (2) without any approximation using a finite volume solver, the number of grid points needed are

$$N \approx Re^{3/2}, \quad (3)$$

with the associated computer memory

$$m \approx 40N^3 \text{ (byte)}. \quad (4)$$

It is therefore computationally expensive to directly compute (1) and (2) as Reynolds number increases. The present study performed a Direct Numerical Simulation (DNS) at Re = 250 and 1,000. The computations at Re = 10,000 are carried out using a Large Eddy Simulation (LES) modelling approach in order to minimize computation cost.

LES Governing Equations

Although the LES methodology was developed in the early 60's by Smagorinsky (1963), it only became a truly engineering tool in the early 90's (Blazek, 2005). The idea behind LES is to capture the large eddies which contribute to the momentum and energy transfer, while the effects of the more homogenous small-scale motions are approximated using a mathematical model. This is achieved by spatially filtering the primitive variables into a large-scale (resolved) and small-scale (unresolved) component. The governing equations are solved for the resolved scale only. This approach significantly reduces computational cost as fewer grid points are required as compared to DNS.

The original Smagorinsky model (Smagorinsky, 1963) uses a constant model coefficient, C_s, to assume the anisotropic part of the subgrid-scale (SGS) tensor. This model has several drawbacks and thus in this study, the dynamic Smagorinsky model proposed by Germano *et. al.* (1991) was employed. The dynamic Smagorinsky model adjusts the model coefficient, C_d, in space and time based on the energy content of the smallest scale eddies. The model constant was evaluated using the least-square minimisation (Lily, 1992).

Numerical algorithm

A brief description of the numerical algorithm is presented in this section. More details of the numerical method can be obtained in Mahesh *et. al.* (2004) and Ham and Iaccarino (2004). In CDP, the Cartesian flow variables (u_i, p) are stored at the centre of the control volume. The face-normal component of the velocity (u_f) is stored at the internal face centre. The solution is time-advanced via a second-order time accurate fractional step semi-discretization of the incompressible Navier-Stokes equations (Kim and Moin, 1985; Zang *et. al.*, 1994; Kim and Choi, 2000),

$$\begin{aligned} & V_p \frac{\hat{u}_{i,p} - u_{i,p}^n}{\Delta t} \\ & + \sum_f u_f^{n+0.5} \left(\frac{u_{i,p}^{n+0.5} + u_{i,nbr}^{n+0.5}}{2} \right) A_f , \\ & = -V_p \frac{\partial p^{n-0.5}}{\partial x_i} \end{aligned} \quad (5)$$

which ensures conservation of discrete kinetic energy. For simplicity, the above equation has excluded both the viscous and SGS tensor, which are included in the actual simulation. Details of the discretization form of these two terms can be found in Mahesh *et. al.* (2004).

On a non-staggered grid, the present collocated formulation will lead to a velocity/pressure decoupling of (5). This decoupling can be overcome by interpolating the Cartesian velocity into the face-normal velocity in the face-normal direction

$$\frac{u_f^{n+1} - u_f^*}{\Delta t} = -\frac{\partial p^{n+0.5}}{\partial n} . \quad (6)$$

A Poisson system for pressure can be obtained by taking the divergence of (6) and enforcing the continuity condition (1). This yields a divergence-free face-normal velocity component

$$\sum_f \frac{\partial p^{n+0.5}}{\partial n} A_f = \frac{1}{\Delta t} \sum_f u_f A_f . \quad (7)$$

Here, the discrete form of the pressure gradient is obtained from the Green-Gauss reconstruction

$$\frac{\partial p}{\partial x_i} = \frac{1}{V_p} \sum_f \frac{p_p + p_{nb}}{2} n_{i,f} A_f . \quad (8)$$

The discretized momentum and Poisson equations are then solved using the HYPRE library and BommerAMG library.

Velocity Boundary Condition

Figures 1 and 2 present the coordinate system and computational domain. The freestream flow is aligned with the z-

axis and the sphere rotation axis is varied between the limits of the x- and z-axis, where the rotation angle, α, is measured from the positive z-axis. The dimensions of the computation domain in this study are:

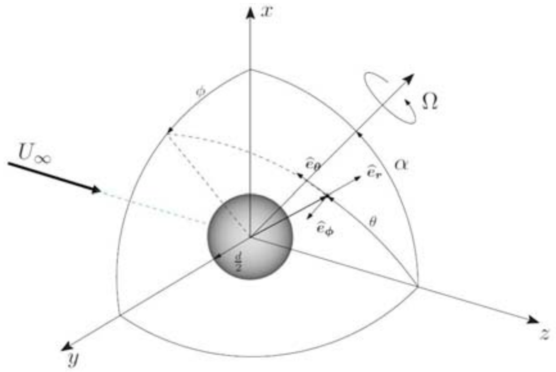

Figure 1: Problem geometry and coordinate system.

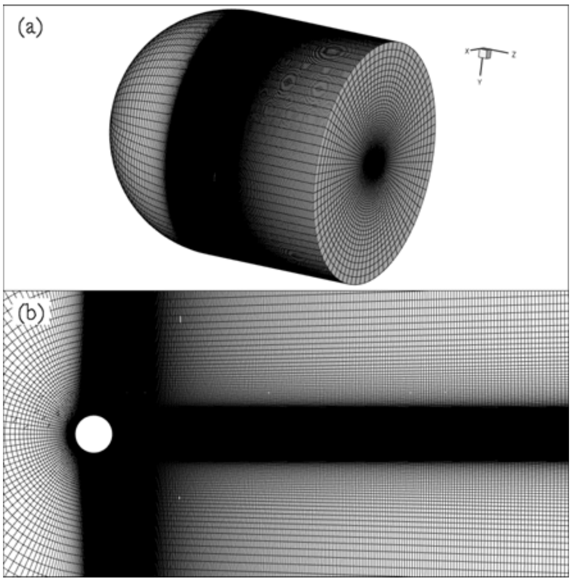

Figure 2: Unstructured-grid Computation domain. (a) Isometric view and (b) plane (x-z) view.

$$x \in [-15,15], \quad y \in [-15,15], \quad z \in [-15,20].$$

Here, (x, y, z) are non-dimensionalized by the sphere diameter, d and the sphere centre is located at (x, y, z) = (0, 0, 0). In total the grid presented in figure 2 comprises 6.94 million control volumes. There are 280 control volumes located in both x- and y-direction, and about 500 control volumes are located downstream of the sphere. The grid is clustered towards the sphere ensuring that there are at least 10 to 15 control volumes located within the boundary layer before separation and enough resolution in the near-wake. At the inlet (z < 0), a Dirichlet boundary condition is prescribed, whereas the boundary condition at the outlet is convective. A no-slip and no-penetration boundary conditions are employed at the sphere surface. For a rotating sphere, the surface velocity distribution is

$$\mathbf{u}\big|_{\partial\Gamma} = \boldsymbol{\Omega} \times \boldsymbol{r}$$

$$\mathbf{u}\Big|_{\partial\Gamma} = \frac{\Omega d}{2}\Big[(-\cos\alpha\sin\phi\sin\theta)\boldsymbol{e}_x + (-\sin\alpha\cos\theta + \cos\alpha\sin\theta\cos\phi)\boldsymbol{e}_y + (-\sin\alpha\sin\phi\sin\theta)\boldsymbol{e}_z\Big] \tag{9}$$

RESULT

The numerical results are presented in ascending Reynolds numbers order. The flow structures are identified using Jeong and Hussain (1995) λ_2 vortex identification method and are presented for all Reynolds numbers considered. Time-averaged quantities of a rotating sphere at Re = 250 and a stationary sphere at Re = 1,000 are presented in their non-dimensional form. Whereas the flow past a rotating sphere at Re = 1,000 and 10,000 are discussed qualitatively.

Re = 250 (DNS)

Figures 3 and 4 present the flow past a streamwise and transversely rotating sphere, respectively, for Re = 250. The flow field is unsteady for these simulation parameters. The flow structures calculated using CDP are in good agreement with those calculated by Kim and Choi (2002), Poon *et. al.* (2007) and Giacobello *et. al.* (2009). Table 1 presents the time-averaged force coefficients and Strouhal numbers from this study together with data in the open literature.

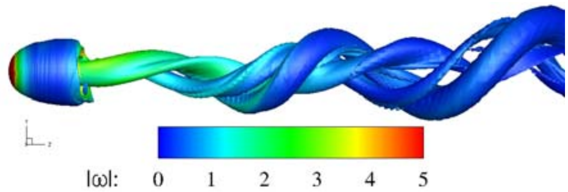

Figure 3: Isosurfaces plot of wake structures at Re = 250, Ω^* = 1.00, α = 0 (streamwise rotation) coloured by the vorticity magnitude.

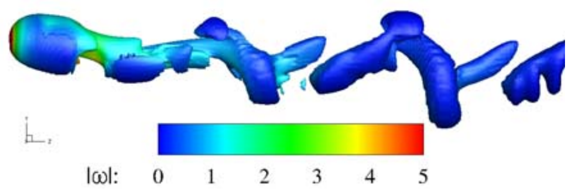

Figure 4: Isosurfaces plot of wake structures at Re = 250, Ω^* = 0.20, α = $\pi/2$ (transverse rotation) coloured by the vorticity magnitude.

CFD Run	C_D	C_L	St
Ω^* = 1.00, α = 0			
CDP (present study)	0.85	0.07	0.10
Kim and Choi (2002)	0.85	0.06	0.09
Poon *et. al.* (2007)	0.85	0.06	0.09
Ω^* = 0.20, α = $\pi/2$			
CDP (present study)	0.76	0.27	0.18
Giacobello *et. al.* (2009)	0.76	0.26	0.18

Table 1: Time-averaged force coefficients and Strouhal number comparison.

Overall, this section demonstrates that CDP can adequately capture the flow physics for a rotating sphere at Re = 250. The discrepancy between CDP and data in the open literature can be attributed to the difference between numerical methods.

Re = 1,000 (DNS)

Ω^* = 0.00

The flow past a stationary sphere at Re = 1,000 is presented in figure 5. The isosurfaces plot resembles the sketch made by Achenbach (1973) for Re = 1,000. In his experimental observation, he noted that the large-scale vortex loops are formed from the separated shear layer in the turbulence regime. As they travel downstream, the loops roll up and then dissipate. On the other hand, the small-scale eddies can be characterized by the presence of a higher frequency component associated with the shear layer instability (Tomboulides and Orszag, 2000). It is also evident that the flow structures become asymmetric at Re = 1,000. This is consistent with Sakamoto and Haniu (1990) and Tomboulides and Orszag (2000) who reported a loss of symmetric at $Re \sim 420$ and Re = 500, respectively.

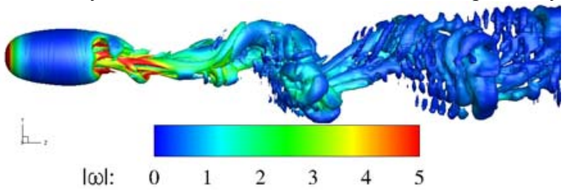

Figure 5: Isosurfaces plot of wake structures at Re = 1,000 coloured by the vorticity magnitude.

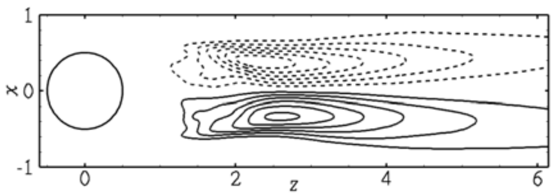

Figure 6: Reynolds stress $\overline{u'_x u'_z}/U_\infty^2$. Contour levels are from -0.035 to 0.035. The dash lines represent negative Reynolds stresses.

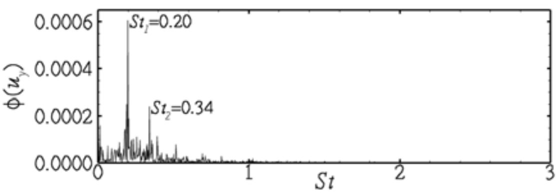

Figure 7: Energy spectrum of u_y versus Strouhal number at (x, y, z) = (0.60, 0.00, 3.00).

CFD Run	C_D	C_L	St_1	St_2
Ω^* = 0.00				
CDP (present study)	0.46	0.01	0.20	0.34
Ploumhans (2002)	0.48	0.00	-	-
T & O (2000)	-	-	0.20	0.35
S & H (1990)	-	-	0.21	0.34
K & D (1988)	-	-	0.20	0.37

Table 2: Time-averaged force coefficients and Strouhal numbers comparison. Sakamoto and Haniu (1972) and Kim and Durbin (1988) data are obtained experimentally.

In the present study, the flow past a stationary sphere has been simulated until the flow fields have reached a statistically steady state. Figure 6 presents one of the six Reynolds stress components for Re = 1,000. In near-wake region, the Reynolds stress is close to 0 which suggests that the boundary layer before separation and the shear layer is laminar and steady. As the shear layer travels downstream, it rolls up and forms vortex loops and thus increases the Reynolds stress levels. The velocity where the shear layer begins to roll up is monitored. The power spectrum of the velocity versus Strouhal number is presented in figure 7. It shows a second higher frequency component at St_2 = 0.34 associated with the shear layer instability (similar to the observation by Tomboulides and Orszag, 2000) together with a lower frequency component at St_1 = 0.20 associated with the large-scale vortex shedding motion. The time-averaged force coefficients and Strouhal numbers agree well with data available in the open literature and are presented in table 2.

Ω^* = 1.00, α = 0

The flow structures for a streamwise rotating sphere at Re = 1,000 and Ω^* = 1.00 are presented in figure 8. It is observed that hairpin structures are shed from the sphere and rotate around the z-axis as they travel downstream. This behaviour was also observed by Kim and Choi (2002) at Re = 300 and Ω^* = 0.10. They also showed that as Ω^* increases, the flow transits into a helical shape. The presence of the hairpin vortices at Ω^* = 1.00 for Re = 1,000 suggests that a higher Ω^* is required to overcome the inertia effect of the flow as Reynolds number increases. In addition, a streamwise rotating sphere slightly increases the vorticity magnitude of the flow over the sphere and in the near-wake region. Furthermore, the shear layer is shortened due to the increase adverse pressure gradient generated by the streamwise rotating sphere.

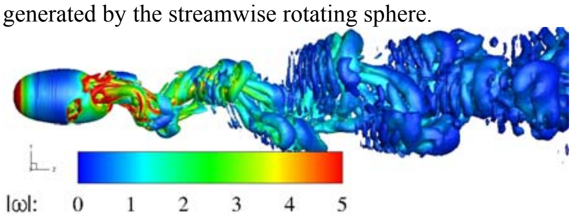

Figure 8: Isosurfaces plot of wake structures at Re = 1,000, Ω^* = 1.00, α = 0 (streamwise rotation) coloured by the vorticity magnitude.

Ω^* = 1.00, α = π/2

Figure 9 presents the flow past a transversely rotating sphere at Re = 1,000 and Ω^* = 1.00. In general, the flow structures are tilted towards the advancing side ($y < 0$) of the sphere and are asymmetric. Vortex loops are formed in the wake region with many small-scale structures are present. Furthermore, the transversely rotating sphere increases the vorticity magnitude of the flow over the sphere. In the near-wake region the flow is found to wrap behind the sphere and forms 2 trailing vortices. This is due to the velocity difference between the sphere surface and the freestream. As the flow on the retreating side ($y > 0$) of the sphere is travelling faster than the advancing side, the separation on the retreating side of the sphere is delayed. A low pressure region is then formed behind the separation on the retreating side. The high pressure flow on the advancing side is thus forced into the low pressure region and forms 2 trailing vortices. The same mechanism can also be found at Re = 250 and Ω^* = 0.20 where the 2 trailing vortices form the “legs” behind the sphere and then transform themselves into "Omega" shape vortex loops as they move downstream (see figure 4). In contrast, at Re = 1,000, the 2 trailing vortices transform into several streamwise threads. The treads then roll up and form vortex loops similar to those observed at Re = 250.

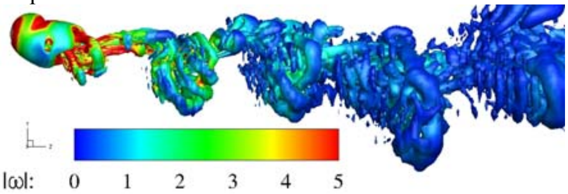

Figure 9: Isosurfaces plot of wake structures at Re = 1,000, Ω^* = 1.00, $\alpha = \pi/2$ (transverse rotation) coloured by the vorticity magnitude.

Re = 10,000 (LES)

Ω^* = 0.00

The simulation for Re = 10,000 was advanced using the flow field calculated at Re = 1,000. At Re = 10,000, a LES was performed in order to reduce computational cost. Again, data was analysed once the flow field reached a statistically steady state. The flow structures past a stationary sphere at Re = 10,000 are presented in figure 10. At this Reynolds number, the wake is completely turbulent. Unlike the simulation at Re = 1,000, vortex rings are observed in the near-wake region and the downstream wake comprises of many small-scale eddies. Furthermore, the wake structures do not show the formation of large-scale vortex loops as observed at lower Reynolds numbers.

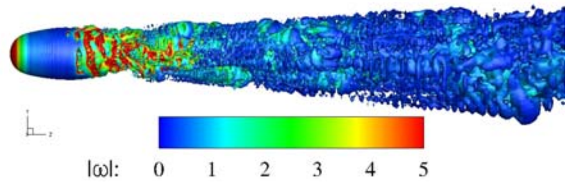

Figure 10: Isosurfaces plot of wake structures at Re = 10,000 coloured by the vorticity magnitude.

The corresponding Reynolds stress shown in figure 11 indicates that the boundary layer before separation and the shear layer is laminar and steady. However, the shear layer instability occurs further upstream compared to Re = 1,000. It is also observed that the location of the maximum Reynolds stress is brought upstream as Reynolds number increases.

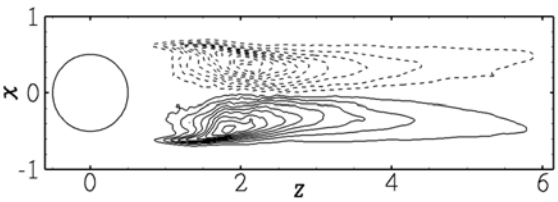

Figure 11: Reynolds stress $\overline{u'_x u'_z} / U_\infty^2$. Contour levels are from -0.035 to 0.035. The dash lines represent negative Reynolds stresses.

At Re = 10,000, velocities are monitored at 2 separation locations: in the near-wake and the far-wake region. The Strouhal numbers correspond to the shear layer instability (St_2) and vortices shedding (St_1) are presented in figure 12 and 13, respectively. The power spectrum reveals a wide range of energy content in the shear layer, which agrees with findings of Yun *et. al.* (2006). The frequency range is reduced as it reaches the far-wake region. In table 3, the time-averaged force coefficients and the Strouhal numbers are presented and all values are with good agreement with data available in the open literature.

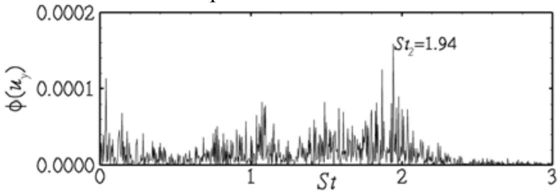

Figure 12: Energy spectrum of u_y versus Strouhal number in the shear layer (x, y, z) = (0.25, 0.54, 1.00).

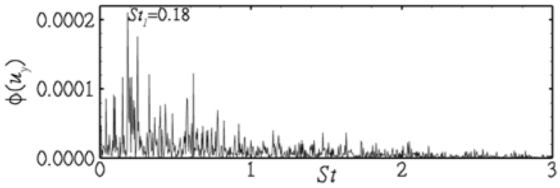

Figure 13: Energy spectrum of u_y versus Strouhal number in the wake region (x, y, z) = (-0.12, -0.59, 3.00).

CFD Run	C_D	C_L	St_1	St_2
Ω^* = 0.00				
CDP (present study)	0.39	0.00	0.18	1.94
Achenbach (1972)	0.41	-	-	-
Yun *et. al.* (2006)	0.39	0.00	0.18	1.78
C & S (2004)	0.39	-	0.19	2.10
K & D (1988)	-	-	0.15	2.02

Table 3: Time-averaged force coefficients and Strouhal numbers comparison. Results from Achenbach (1972) and Kim and Durbin (1988) were obtained experimentally.

Ω^* = 1.00, $\alpha = \pi/2$

Figure 14 presents the flow past a transversely rotating sphere at Re = 10,000 and Ω^* = 1.00. As mentioned, a transversely rotating sphere experiences a negative "Robins-Magnus" lift force at $Re = O(10^4)$. Davies (1949) attributed this behaviour to the laminar-turbulent boundary transition. At sufficient high Reynolds number, the addition effect of the rotating surface can trip the boundary layer on the advancing side of the sphere to turbulent. This causes a delay in the separation point on the advancing side and affects the pressure recovery behind the sphere. Therefore, a negative "Robins-Magnus" lift force was observed. The flow visualisation in the present study confirms that the boundary layer on the advancing side is tripped at sufficient high Reynolds numbers. However, a more detail analysis must be performed to verify the present simulation parameters indeed lead to a negative "Robins-Magnus" effect.

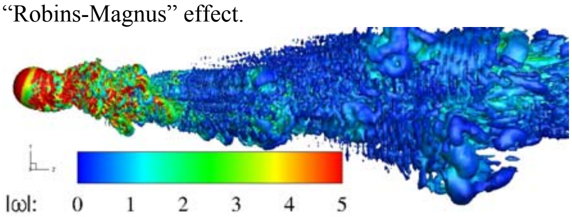

Figure 14: Isosurfaces plot of wake structures at Re = 10,000, Ω^* = 1.00, $\alpha = \pi/2$ (transverse rotation) coloured by the vorticity magnitude.

CONCLUSION

Numerical studies for the flow past a stationary and rotating sphere were performed using the finite volume code CDP. CDP shows excellent agreement with the data available in the open literature for flow past a rotating sphere at $Re = 250$ and a stationary sphere at $Re = 1{,}000$ and 10,000. Flow visualization was presented for a rotating sphere at high Reynolds numbers. At $Re = 1{,}000$, $\Omega^* = 1.00$ and $\alpha = 0$, hairpin vortices were observed and they rotate around the streamwise axis as they convect downstream. The appearance of hairpin vortices at $\Omega^* = 1.00$ and $Re = 1{,}000$ suggests that a higher Ω^* is required to overcome the inertia effect of the flow at higher Reynolds number in order to have a helical flow structure. At $Re = 1{,}000$, $\Omega^* = 1.00$ and $\alpha = \pi/2$, vortex loops with many small-scale structures were observed. The mechanism connecting the vortex loops is similar to those observed at $Re = 250$. The rotating sphere also increases the vorticity magnitude of the flow over the sphere. At $Re = 10{,}000$, $\Omega^* = 1.00$ and $\alpha = \pi/2$, the boundary layer on the advancing side of the sphere is tripped and flow separation is thus delayed. This in turn affects the pressure recovery behind the sphere and thus affects the "Robins-Magnus" lift force.

REFERENCES

ACHENBACH, E., (1972), "Experiments on the flow past spheres at very high Reynolds numbers", *J. Fluid Mech.*, **54**, 565.

ACHENBACH, E., (1974), "Vortex shedding from sphere", *J. Fluid Mech.*, **62**, 209-221.

BLAZEK, J., (2005), "Chapter 7: Turbulence Modelling", *In: Computational Fluid Dynamics: Principles and Applications*, 227-270. Elsevier.

CONSTANTINESCU, G. and SQUIRES, K., (2004), "Numerical investigation of flow over a sphere in the subcritical and supercritical regimes", *Phys. Fluids*, **16**, 1449-1466.

DAVIES, J. M., (1949), "The aerodynamics of a golf balls", *J. Appl. Phys.*, **20**, 821-828.

GERMANO, M., PIOMELLI, U., MOIN, P., and CABOT, W., (1991), "A dynamic subgrid-scale eddy-viscosity model", *Phys. Fluids*, **3**, 1760-1765.

GERMANO, M., (1992), "Turbulence: The filtering approach", *J. Fluid Mech.*, **238**, 325-336.

GIACOBELLO, M., OOI, A. and BALACHANDAR, S., (2009), "Wake structure of a transversely rotation sphere at moderate Reynolds numbers", *J. Fluid Mech.*, **621**, 103-130.

HAM, F., and IACCARINO, G., (2004), "Energy conservation in collocated discretization schemes on unstructured meshes", *Annaual Research Brief 2004*, Centre for Turbulent Research, NASA ames/Stanford Univ., 3-14.

HOSKIN, N. E., (1955), "The laminar boundary layer on a rotating sphere" *In: Fifty years of boundary layer research*, 127-131, Braunschweig.

JIMÉNEZ, J., (2003), "Computing high-Reynolds-number turbulence: will simulations ever replace experiments?", *J. Turbulence*, **4**, 22.

JEONG, J. and HUSSAIN, F., (1995), "On the identification of a vortex", *J. Fluid Mech.*, 2**85**, 69-94.

JOHNSON, T. A. and PATEL, V. C., (1999), "Flow past a sphere up to a Reynolds number of 300", *J. Fluid Mech.*, **378**, 19-70.

KIM, D. and CHOI, H., (2000). "A second-order time accurate finite volume method for unsteady incompressible flow on hybrid unstructured grids", *J. Comput. Phys*, **162**, 411-428.

KIM, D. and CHOI, H., (2002) "Laminar flow past a sphere rotating in the streamwise direction", *J. Fluid Mech.*, **461**, 365-386.

KIM, H, J., and DURBIN, P. A., (1988), "Observation of the frequency in a sphere wake and of drag increase by acoustic excitation", *Phys. Fluids*, **31**, 3260.

KIM, J. and MOIN, P., (1985), "Application of a fractional-step method to incompressible Navier-Stokes equations", *J. Comput. Phys*, **59**, 308-323.

KUROSE, R., & KOMORI, S., (1999) "Drag and lift forces on a rotating sphere in a linear shear flow", *J. Fluid Mech.*, **384**, 183-206

LILLY, D. K., (1992), "A proposed modification of the Germano subgrid-scale closure method", *Phys. Fluids*, **4**, 633-635.

LUTHANDER, S., and RYDBERG, A., (1935), "Experimentelle untersuchungen uber den luftwiderstand bei einer um eine mit der windrichtung paraleel achse rotierenden kugel", *Phys. Z*, **36**, 552-558.

MACCOLL, J. H., (1928), "Aerodynamics of a spinning sphere". *J. Roy. Aero. Soc.*, **32**, 777-798.

MAHESH, K., CONSTANTINESCU, G., and MOIN, P., (2004), "A numerical method for large eddy simulation in complex geometries", *J. Comp. Phys*, **197**, 215-240

MITTAL, R., (1999), "A Fourier-Chebyshev spectral collocation method for simulating flow past spheres and spheroids", *Int. J. Numer. Meth. Fluids*, **30**, 921-937.

NIAZMAND, H., & RENKSIZBUKUT, M., (2003), "Surface effects on transient three-dimensional flows around rotating spheres at moderate Reynolds numbers", *Comp. Fluids*, **32**, 1405-1433.

POON, K. W., OOI, A., GIACOBELLO, M., PERALTA, C., and MELATOS, A., (2007)., "Numerical simulations of flow past a stationary and rotating sphere", *16th Australasian Fluid Mechanics Conference*, Gold Coast, Queensland, Australia, 870-875.

PLOUMHANS, P., WINCKELMANS, G. S., SLAMON, J. K., LEONARD, A., and WARREN, M. S., (2002), "Vortex Methods for direct numerical simulation of three-dimensional bluff body flow: Application to the sphere at *Re* = 300, 500, and 1000", *J. Comp. Phys.*, **178**, 427-463.

RUBINOW, S. I., and KELLER, J. B., (1961), "The transverse force on a spinning sphere moving in a viscous fluid", *J. Fluid Mech.*, **11**, 447-459.

SAKAMOTO, H. and HANIU, H., (1990), "A study on vortex shedding from spheres in a uniform flow", *ASME: J. Fluids Eng.*, **112**, 386-392.

SMAGORINSKY, J., (1963), "General circulation experiments with the primitive equations", *Monthly weather review*, **91**, 99-164.

TANEDA, S., (1956), "Experiment Investigation of the wake behind a sphere at low Reynolds numbers", *J. Phys. Soci. Japan*, **11**, 1104-1108.

TANEDA, S., (1978), "Visual observation of flow past a sphere at Reynolds numbers between 10^4 and 10^6", *J. Fluid Mech.*, **85**, 187-192.

TOMBOULIDES, A. G., and ORSZAG, S. A., (2000), "Numerical investigation of transitional and weak turbulent flow past a sphere", *J. Fluid Mech.*, **416**, 45-73.

YOU, C. F., QI, H. Y., and XU, X. C., (2003), Lift force on rotating sphere at low Reynolds numbers and high rotational speed. *ACTA Mechanica Sinica*, **19**, 300-307.

YUN, G., KIM, D., and CHOI, H., (2006), "Vortical structures behind a sphere at subcritical Reynolds numbers", *Phys. Fluids*, **18**, 015102.

